



Contents lists available at ScienceDirect

Atmospheric Environment

journal homepage: <http://www.elsevier.com/locate/atmosenv>

Rain rate and radon daughters' activity

Carlo Bottardi^{a,c}, Matteo Albéri^{a,b}, Marica Baldoncini^{a,b}, Enrico Chiarelli^{a,c},
Michele Montuschi^{a,c}, Cassandra Giulia Cristina Raptis^{a,c}, Andrea Serafini^{a,c},
Virginia Strati^{a,c,d,*}, Fabio Mantovani^{a,c}

^a Department of Physics and Earth Sciences, University of Ferrara, Via Saragat 1, 44121, Ferrara, Italy

^b INFN, Legnaro National Laboratories, Viale dell'Università, 2, 35020, Legnaro, Padua, Italy

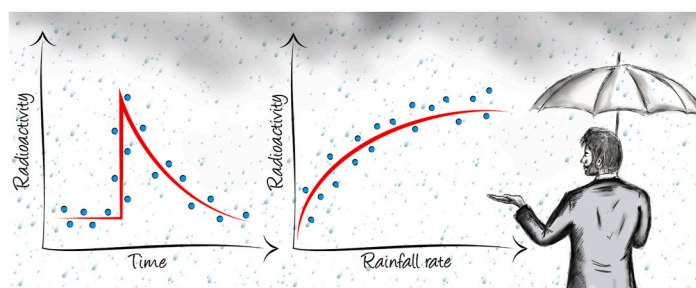
^c INFN, Ferrara Section, Via Saragat 1, 44121, Ferrara, Italy

^d GeoExplorer Impresa Sociale S.r.l., Via E. Vezzosi 15, 52100, Arezzo, Italy

HIGHLIGHTS

- Every impulse of rain produces a sudden increase of ^{214}Pb gamma activity.
- A reproducible model reconstructs the temporal evolution of the ^{214}Pb count rate.
- For a fixed rainfall amount longer events correspond to higher ^{214}Pb content.
- Gamma-ray spectroscopy can discriminate between irrigation and rainfall.
- Increase of radon daughters' activity depends on the square root of the rain rate.

GRAPHICAL ABSTRACT



ARTICLE INFO

Keywords:

Rain induced gamma activity
Rain rate
Rain median diameter
Rain radon daughters' content
 ^{214}Pb count rate modelling
Rain ^{214}Pb activity density

ABSTRACT

During a precipitation a transient increase of gamma activity is generated by ^{214}Pb and ^{214}Bi , daughters of atmospheric ^{222}Rn , which are collected by rain droplets and brought to the ground. A continuous monitoring of this gamma radiation can be an efficient alternative to a ^{222}Rn direct measurement in clouds and allows for estimating rain-induced variations in environmental gamma radiation.

This work presents the results of a seven months proximal gamma-ray spectroscopy experiment, specifically tailored for gathering reliable and unbiased estimates of atmospheric ^{214}Pb gamma activity related to rainfalls. We developed a reproducible model for reconstructing the temporal evolution of the ^{214}Pb net count rate during rain episodes as function of the rain rate. The effectiveness of the model is proved by an excellent linear correlation ($r^2 = 0.91$) between measured and estimated ^{214}Pb count rates. We observed that the sudden increase of ^{214}Pb count rates (ΔC) is clearly related to the rain rate (R) by a power law dependence $\Delta C \propto R^{0.50 \pm 0.03}$. We assessed that the radon daughter ^{214}Pb content (G) of the rain water depends on the rain rate with $G \propto 1/R^{0.48 \pm 0.03}$ and on the rain median volume diameter (λ_m) with $G \propto 1/\lambda_m^{2.2}$. We proved that, for a fixed rainfall amount, lower is the rainfall intensity (i.e. the longer is the rain duration), higher is the radon daughters' content of the rain water.

* Corresponding author. Department of Physics and Earth Sciences, University of Ferrara, Via Saragat 1, 44121, Ferrara, Italy.
E-mail address: strati@fe.infn.it (V. Strati).

<https://doi.org/10.1016/j.atmosenv.2020.117728>

Received 15 January 2020; Received in revised form 14 June 2020; Accepted 21 June 2020

Available online 3 July 2020

1352-2310/© 2020 Elsevier Ltd. All rights reserved.

1. Introduction

In the last decades the transient increase of gamma activity occurring during and after a precipitation has been widely observed and studied as a relevant cause of variation of the environmental gamma radiation background (Minato, 1980; Yakovleva et al., 2016). The comprehension of such a variation is necessary in order to establish reliable and proper thresholds for radiological emergencies (Melintescu et al., 2018).

^{222}Rn is a radioactive noble gas with poor chemical reactivity. Thanks to its 3.82 days half-life, ^{222}Rn lives long enough to be of significance to events related to turbulence (~ 1 h time scale) but it lives also quite little to have a high concentration gradient through the lower troposphere (Baldoncini et al., 2017; Baskaran, 2016; Wilkening, 1981). These properties make ^{222}Rn a widespread atmospheric tracer, together with anthropogenic radionuclides (mainly derived from open-air nuclear weapon testing and occasional nuclear accidents) and cosmogenic radionuclides produced by the interaction of cosmic rays with the gaseous components of the atmosphere (Froehlich, 2009; Turekian and Graustein, 2003). Monitoring atmospheric ^{222}Rn has plenty of applications in environmental sciences, including the comprehension of air vertical mixing processes (Chambers et al., 2016) and the testing of meteorological models describing the transport of pollutants (Chambers et al., 2015), with consequent implications on studies related to climate change and removal processes of gases and aerosols (Jacob and Prather, 1990; Jacob et al., 1997).

The continuous ^{222}Rn monitoring at low concentrations, as found in the atmosphere, is more challenging than monitoring its gamma emitting daughters ^{214}Pb and ^{214}Bi (Barbosa et al., 2017). Although various radionuclides such as ^7Be , ^{212}Pb and ^{210}Pb are observed in precipitation, the main sources of rain-induced gamma activity at ground level are ^{214}Pb and ^{214}Bi , produced in the decay of atmospheric ^{222}Rn and brought to the ground after being collected by rain droplets (Bosew et al., 2017).

Continuous and spatially distributed measurements of ^{214}Pb and ^{214}Bi gamma activity can be a powerful experimental technique in meteorology. Indeed, increased dose rates due to wet deposited ^{222}Rn gamma emitting progeny can provide insights into air mass origin and regional characteristics of precipitations. In previous studies (Inomata et al., 2007; Mercier et al., 2009; Paatero, 2000; Yoshioka, 1992) ^{214}Pb and ^{214}Bi gamma activity measurements allowed for instance to demonstrate that a cloud with marine (continental) origin is usually characterized by a ^{222}Rn concentration lower (higher) with respect to the average concentration. Furthermore, since in precipitation water the temporal evolution of the $^{214}\text{Pb}/^{214}\text{Bi}$ activity ratio is governed only by the half-lives of the two radionuclides ($t_{1/2}^{214\text{Pb}} = 26.8 \text{ min}$; $t_{1/2}^{214\text{Bi}} = 19.9 \text{ min}$), the $^{214}\text{Pb}/^{214}\text{Bi}$ activity ratio measurement enables the determination of rain and snow age (Greenfield et al., 2008) and can shed light into advection, convection and diffusion processes in the troposphere (Porstendörfer, 1994; Shapiro and Forbes-Resha, 1975).

Measuring the gamma activity of ^{222}Rn progeny in precipitation has also applications in health studies, earthquake predictions (Harrison et al., 2014), cosmic rays research and radiation levels monitoring. Eatough and Henshaw (1995) estimated that 2% of non-melanoma skin cancers in the UK may be caused by environmental radon exposure, which may be increased as a result of rain-out processes (Kendall and Smith, 2002). In the last years many studies were performed with the aim of establishing a correlation between seismic activity and increase of outdoor radon and radon progeny concentration (Friedmann, 2012; Karangelos et al., 2005; Riggio and Santulin, 2015; Woith, 2015). Such correlation has not yet been proved but the advancement in the field cannot disregard precipitation as a source of additional gamma activity, which could give rise to false positives and consequently fake

earthquake alarms. Rainfall induced gamma activity represents also a source of background in measuring low energy secondary cosmic rays (Muraki et al., 2004) and it is particularly relevant when radiation from anthropic sources must be discriminated from that of natural origin. Indeed, radiation monitoring of nuclear facilities (Mercier et al., 2009) and detection of illicit movement of special nuclear material (Livesay et al., 2014), generally require the assessment of environmental radiation at levels as low as a few percent of the natural background (Minato, 1980).

In this work we present the results of a proximal gamma-ray spectroscopy experiment aimed at studying the ^{214}Pb gamma activity temporal profile in relation to rainfalls. The experiment was performed by installing an agro-meteorological station, provided with a traditional bucket rain gauge, and a custom gamma-ray spectroscopy station equipped with a 1 L sodium iodide (NaI) scintillator, in an agricultural test field. Meteorological and radiometric data were continuously acquired for 7 months, temporally aligned and analysed in order to address the following research questions:

- (i) Can a reproducible mathematical model reconstruct the temporal profile of the rain-induced ^{214}Pb gamma activity?
- (ii) What is the dependence between the sudden increase of ^{214}Pb count rates observed during every rain and the rain rate?
- (iii) Can the radon daughters' content of rain water be quantitatively inferred from the rain rate?
- (iv) Can proximal gamma-ray spectroscopy be a valuable tool to have insights on the radioactivity content of rain droplets?

2. Materials and methods

2.1. Modelling rain induced activity

This work focuses on the reconstruction of the gamma signal generated by ^{214}Pb , which has a half-life of 26.8 min (comparable to rain time-scales) and which activity has been already monitored in previous studies in relation to rains (Inomata et al., 2007; Livesay et al., 2014; Mercier et al., 2009).

^{222}Rn is a gaseous parent radionuclide which triggers the decay chain described in Fig. 1. Since during an alpha decay few electrons are stripped from the recoil of the parent atom (Stevanović et al., 2004), the results of ^{222}Rn decay is a charged ion $^{218}\text{Po}^+$ in $\sim 90\%$ of decays (Hopke, 1989; Porstendörfer, 1994). Due to its lower first ionization potential (8.34 eV) with respect to the atmospheric surrounded molecules elements, $^{218}\text{Po}^+$ may prevent the process of total neutralization, leaving the atom in a charged state (Fig. 2). The fates of $^{214}\text{Pb}^+$ and $^{214}\text{Bi}^+$, having ionization potentials 7.42 and 7.29 eV respectively, are expected to be the same (Castleman, 1991). Therefore, radon daughters adhere to the water molecules in the air or react with vapours and trace gases in less than 1 s. The obtained small clusters (0.5–5 nm), characterized by a high mobility, attach to aerosol in time scale of 1–100 s forming a “radioactive aerosol” (diameter ~ 100 – $300 \mu\text{m}$) (Mostafa et al., 2020) which in turn attaches to droplets. These in-cloud scavenging (rainout) processes are responsible for the radioactive enrichment into rain droplets with an efficiency higher than below-cloud scavenging (washout) (Fig. 2). ^{222}Rn and its progenies are considered in secular equilibrium in the clouds (Greenfield et al., 2008; Takeyasu et al., 2006), but when rain droplets begin their descent to the ground the equilibrium is broken.

The model developed for reconstructing the ^{214}Pb gamma activity time series at ground level as function of the rainfall rate is based on the following assumptions.

- The increase of ^{214}Pb gamma activity at ground level is due only to the decay of ^{214}Pb attached to raindrops.
- For a single rain episode, the temporal evolution of the ^{214}Pb rain-induced gamma activity depends only on the rainfall rate. Two factors affecting the ^{214}Pb concentration are considered negligible: the contribution due to the below-cloud scavenging (Greenfield et al., 2008) and the radon-aerosol heterogeneities in the clouds. Indeed, since the system radon-aerosol depends on cloud history, the efficiency of in-cloud scavenging changes among different rain episodes, but it can be considered homogenous for a rain of a few hours (see Section 2.3).
- The ^{214}Pb net background count rates (describing the not rain-induced gamma activity) before and after the rain time are in principle different. This is reasonable since precipitated water soaks the soil, attenuating the signal produced by the ^{214}Pb present in the ground.

In the presented model the temporal bin has a width of 0.25 h corresponding to the experimental temporal resolution of synchronized radiometric and rainfall data. However, the model is independent from this choice, since the data collected in a single bin are associated to its centre as a delta function. Given a rain bin (i.e. bin with a non-zero rainfall amount) separated from the previous one by at least 9.5 h, a rain Episode is defined as four consecutive Periods (P) described as follows (Fig. 3):

- P1 covers the 5 h (see Section 2.3) before the beginning of the rainfall and permits the estimation of the ^{214}Pb background net count rate $C_{\text{Bkg}}^{\text{Before}}$;
- P2 starts and ends respectively at the first and last temporal bins for which a non-zero rainfall amount is measured. Note that this Period can include more rain bins separated by no rainfall time intervals (e.g. Episode 1 in Fig. 8) shorter than 9.5 h;
- P3 follows the end of P2 for a duration of 4.5 h, corresponding to ~ 10 ^{214}Pb half-lives, necessary to let the ^{214}Pb net count rate decrease exponentially to the after-rain background value $C_{\text{Bkg}}^{\text{After}}$;
- P4 covers the 5 h after the end of P3 and permits to estimate the ^{214}Pb background net count rate $C_{\text{Bkg}}^{\text{After}}$.

With the purpose of describing the gamma ^{214}Pb net count rate time series during a rain episode, two signal components must be considered: (i) the rain induced source term and (ii) the ^{214}Pb radioactive decay term. The source term in the ^{214}Pb Bateman equation due to the ^{218}Po decay is neglected since its half-life (3.1 min) is sufficiently short that it will have decayed to 0.01% of its initial activity by the precipitation age (~ 30 min), i.e. the average time between the removal of the ^{222}Rn progeny from secular equilibrium by rain and their deposition on the ground (Greenfield et al., 2008). The description of the ^{214}Bi net count rate time series during a rain episode would, instead, require an additional time dependent source term due to the ^{214}Pb decays and, as a consequence, add an additional source of uncertainty.

The variation in time of the number of ^{214}Pb nuclei $N_{\text{Pb}}(t)$ per unit of surface dS can be written as:

$$\frac{dN_{\text{Pb}}(t)}{dS \cdot dt} = + \frac{dN_{\text{Pb}}^{\text{Rain}}(t)}{dS \cdot dt} - \lambda_{\text{Pb}} \cdot \frac{dN_{\text{Pb}}(t)}{dS} \quad (1)$$

where $dN_{\text{Pb}}^{\text{Rain}}$ is the increase in ^{214}Pb nuclei associated to the rain deposition and $\lambda_{\text{Pb}} = 1/\tau_{\text{Pb}} = 4.28 \cdot 10^{-4} \text{ s}^{-1} = 1.54 \text{ h}^{-1}$ is the ^{214}Pb decay constant which rules the exponential decay. The rain-induced source term $\frac{dN_{\text{Pb}}^{\text{Rain}}}{dS \cdot dt}$ can be described as a function of the rain rate $R \left[\frac{\text{mm}}{\text{h}} \right]$:

$$\frac{dN_{\text{Pb}}^{\text{Rain}}(t)}{dS \cdot dt} = n \cdot v_{\text{term}} \cdot N_{\text{Pb}}^{\text{Drop}} = \frac{R}{V_G} \cdot N_{\text{Pb}}^{\text{Drop}} \quad (2)$$

where $n \left[\frac{\text{drops}}{\text{m}^3} \right]$ is the density at ground level of number of raindrops having identical size, $N_{\text{Pb}}^{\text{Drop}} \left[\frac{\text{Pb nuclei}}{\text{drop}} \right]$ is the number of ^{214}Pb nuclei in a raindrop having volume $V_G [\text{m}^3]$ and $v_{\text{term}} \left[\frac{\text{m}}{\text{s}} \right]$ is the raindrop terminal velocity. Since in principle $N_{\text{Pb}}^{\text{Drop}}$ can depend on the rain rate R , the rain induced source term is not expected to linearly scale with R but can be parameterized as a power law of the rain rate R with exponent d :

$$\frac{dN_{\text{Pb}}^{\text{Rain}}(t)}{dS \cdot dt} \sim R^d \quad (3)$$

As the efficiency, the position and the field of view of the Proximal Gamma Ray (PGR) spectroscopy station do not change over time, the footprint area of PGR measurements can be considered constant and having a $\sim 25 \text{ m}$ radius. Consequently, the gamma count rate increase $\Delta C [\text{cps}]$ recorded in a time interval $\Delta T [\text{h}]$ is directly proportional to the number of ^{214}Pb nuclei accumulated to the ground during the same time:

$$\frac{\Delta N_{\text{Pb}}^{\text{Rain}}}{\Delta T} \propto \frac{\Delta C}{\Delta T} = A \cdot R^d \quad (4)$$

where $A \left[\frac{\text{cps}}{\text{mm}^d \text{h}^{1-d}} \right]$ is a proportionality factor that depends on the response of the 1 L NaI(Tl) detector installed in the PGR station and on in-cloud ^{222}Rn concentration.

This theoretical background can be also formulated in terms of activity density $G \left[\frac{\text{cps}}{\text{mm}} \right]$, corresponding to the ^{214}Pb gamma activity in a rainwater layer of thickness $\Delta z [\text{mm}]$, accumulated on the ground in a time interval ΔT by a rainfall of rate R ,

$$\frac{1}{R} \frac{\Delta C}{\Delta T} = \frac{\Delta C}{\Delta z} = G = A \cdot R^{d-1} \begin{cases} \text{if } 0 < d < 1 \rightarrow G \text{ is inversely correlated with } R \\ \text{if } d = 1 \rightarrow G \text{ is independent from } R \\ \text{if } d > 1 \rightarrow G \text{ is positively correlated with } R \end{cases} \quad (5)$$

For a rain occurring in a single bin with duration $\Delta T = t_2 - t_1 = 0.25 \text{ h}$ (Fig. 4) it is assumed that the rain has fallen instantaneously to the ground at $t = t_1 + \frac{0.25 \text{ h}}{2}$. At $t < t_1 + \frac{0.25 \text{ h}}{2}$ the ^{214}Pb net count rate $C(t) [\text{cps}]$ is expected to be equal to the background count rate before the rain $C_{\text{Bkg}}^{\text{Before}}$. At the beginning of the rain at $t = t_1 + \frac{0.25 \text{ h}}{2}$, $C(t)$ has a sharp increase due to the rain-induced activity source term ΔC . At $t > t_1 + \frac{0.25 \text{ h}}{2}$, $C(t)$ is then expected to asymptotically approach the after-rain background value $C_{\text{Bkg}}^{\text{After}}$. The temporal evolution of the ^{214}Pb net count rate $C(t)$ shown in

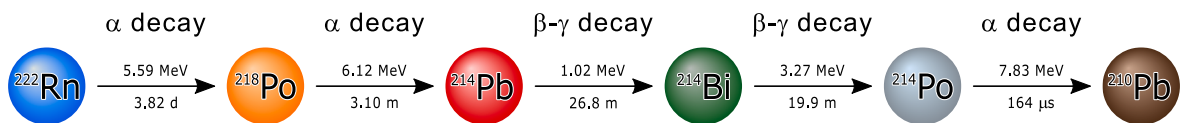


Fig. 1. Simplified ^{238}U decay sub-chain from ^{222}Rn to ^{210}Pb comprising 3 α decays and 2 β - γ decays. The decay channels with branching fractions $< 0.05\%$ are excluded. For each α or β - γ decay (horizontal arrow) the Q-value in MeV and the half-life ($d = \text{day}$, $m = \text{minute}$, $\mu\text{s} = 10^{-6}$ seconds) of the father nucleus are reported. The β - γ decay used in the model is the one transforming ^{214}Pb into ^{214}Bi with the most intense gamma rays having characteristic energies of 295 keV and 352 keV, with the latter chosen for the estimation of the experimental ^{214}Pb net photopeak count rate.

Fig. 4 can therefore be written as:

$$\begin{cases} C(t) = C_{Bkg}^{Before} & \text{with } t < t_1 + \frac{0.25 h}{2} \\ C(t) = \Delta C \cdot e^{-\lambda_{pb} \left[t - \left(t_1 + \frac{0.25 h}{2} \right) \right]} + C_{Bkg}(t) & \text{with } t_1 + \frac{0.25 h}{2} \leq t < t_2 + \frac{0.25 h}{2} \\ C(t) = \Delta C \cdot e^{-\lambda_{pb} \left[t - \left(t_2 + \frac{0.25 h}{2} \right) \right]} + C_{Bkg}^{After} & \text{with } t \geq t_2 + \frac{0.25 h}{2} \end{cases} \quad (6)$$

where $\Delta C[\text{cps}] = \Delta T \cdot A \cdot R^d$ is the sudden increase of count rate associated to the single impulse of rainfall.

In order to develop a theory adequate for describing an episode which rain lasts for n temporal bins with a ΔT width, characterized by R_i rain rates, ΔC_i sudden increase of count rate have to be introduced, with:

$$\Delta C_i = \Delta T \cdot A \cdot R_i^d, 1 \leq i \leq n \quad (7)$$

Under the assumption of constant radon (and radon progenies) concentration in clouds during a given rain episode, the A scaling factor and the exponent d are assumed to be constant during the episode duration, but they can vary from one rain episode to another.

Considering that the ^{214}Pb background net count rates before (C_{Bkg}^{Before}) and after (C_{Bkg}^{After}) are not necessarily equal, a time dependent background $C_{Bkg}(t)$ in period P2 is evaluated on the basis of a linear trend describing the transition from C_{Bkg}^{Before} to C_{Bkg}^{After} (Fig. 3). Consequently, the ^{214}Pb net count rate time series can be mathematically described by the equations in Table 1. Fig. 3 shows the modelling of the ^{214}Pb net count rate $C(t)$ for a rain episode with a P2 including multiple temporal bins with a non-zero rainfall amount.

2.2. Experimental site and setup

The experiment was performed in the period 4 April - 2 November, 2017 in a $40 \times 108 \text{ m}^2$ agricultural test field of the Acqua Campus, a research centre of the Emiliano-Romagnolo Canal (CER) irrigation district in the Emilia Romagna region, Italy.

The experimental setup (Fig. 5a) consisted of an agro-meteorological station (MeteoSense 2.0, Netsens) and a custom PGR spectroscopy station. The agro-meteorological station measured air temperature [$^{\circ}\text{C}$], relative air humidity [%], wind speed [$\frac{\text{m}}{\text{s}}$], and rainfall amount [mm]. The PGR station comprised a 1 L NaI(Tl) scintillator providing a continuous log of individual energy depositions and corresponding detection times. By placing the detector at a 2.25 m height, PGR spectroscopy provided soil moisture measurements with a $\sim 25 \text{ m}$ footprint radius (Baldoncini et al., 2018a; Strati et al., 2018). Thanks to the installation of a solar panel and a GPRS antenna, both stations were self-powered and web connected. A dedicated software was developed to remotely pre-process the data for synchronizing meteorological and radiometric observations in a unique time-referenced dataset having a 0.25 h temporal resolution.

As ^{40}K , ^{238}U and ^{232}Th amounts in the soil were constant, temporal variations in measured gamma spectra could be ascribed to: (i) changes in soil and biomass water content, extensively studied in (Baldoncini et al., 2019), (ii) changes in atmospheric ^{222}Rn , (iii) changes in cosmic radiation levels and (iv) rain-induced gamma activity, which could be traced by monitoring the ^{214}Pb net photopeak count rate. In absence of rain the net number of events recorded in the ^{214}Pb photopeak area was attributable to gamma radiation emitted in the decay of ^{214}Pb distributed in the soil (Fig. 5b and c). In presence of rainfall ^{214}Pb radionuclides brought to ground by raindrops increase the ^{214}Pb gamma activity at ground level and, in turn, the ^{214}Pb photopeak net area (Fig. 5d and e).

The experimental setup and conditions were specifically tailored for gathering reliable and unbiased estimates of the ^{214}Pb activity at ground level and for studying its time series in relation to rainfall episodes. The Acqua Campus research centre has been identified as an ideal site for hosting the experiment since irrigation amounts were carefully

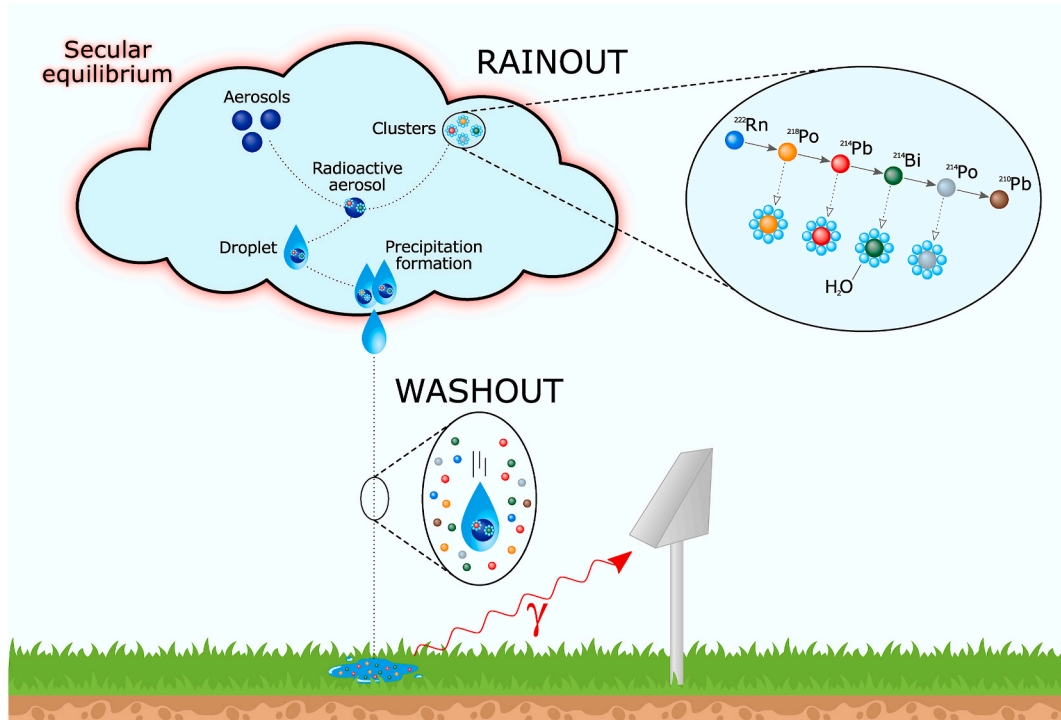


Fig. 2. Scheme of the rainout (i.e. in-cloud scavenging) and washout (i.e. below-cloud scavenging) radioactivity charge mechanisms of raindrops. The increasing of gamma signal can be detected by a permanent gamma ray spectroscopy station.

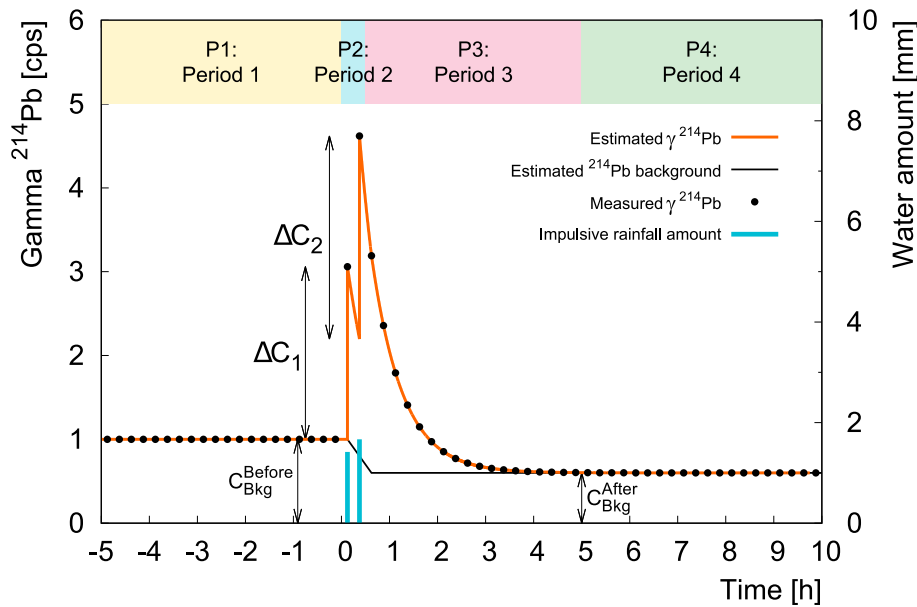


Fig. 3. Temporal evolution of the ^{214}Pb net counts during the four Periods (P) described in Section 2.1. The two consecutive impulsive rains (light blue bars) produce the count rate increase ΔC_1 and ΔC_2 . The black dots and the orange line represent the measured and the estimated ^{214}Pb net count rates respectively. The black line describes the estimated temporal evolution of the ^{214}Pb background net counts during P2 and P3. (For interpretation of the references to colour in this figure legend, the reader is referred to the Web version of this article.)

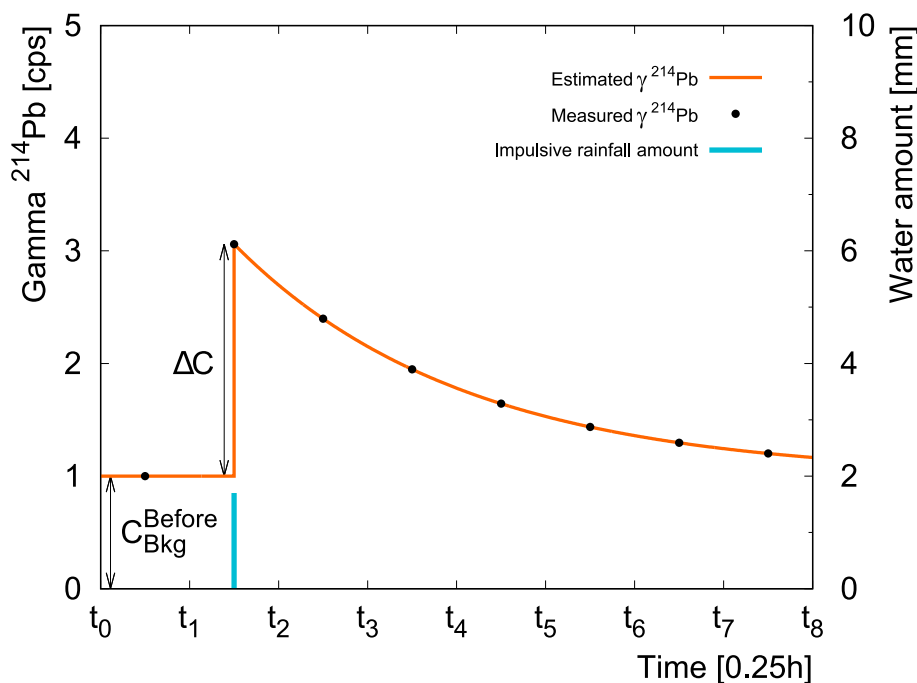


Fig. 4. Temporal evolution of the ^{214}Pb net count rate time series during an impulsive rain (light blue bar) occurring in a single temporal bin and producing a count rate increase ΔC . The black dots and the orange line represent the measured and the estimated ^{214}Pb net count rates respectively. Before the rain, the ^{214}Pb net count rate is equal to the estimated background value $C_{\text{Bkg}}^{\text{Before}}$. When rainfall stops the ^{214}Pb net count rate follows an exponential decrease ruled by the ^{214}Pb decay constant until it reaches the after-rain background asymptotic value $C_{\text{Bkg}}^{\text{After}}$. (For interpretation of the references to colour in this figure legend, the reader is referred to the Web version of this article.)

monitored and logged. The PGR station provided continuous measurements over a 7 months data-taking period with a 94.8% duty cycle overlapping with synchronized agro-meteorological acquisitions, including rainfall amount data relevant for this study. The 1 L detector volume allowed for recording good counting statistics with a sampling frequency adequate for modelling the plateau, peak and exponential decay phases of the rain-induced ^{214}Pb gamma activity temporal dynamics (see Table 3 and Fig. 8). Even if cosmic radiation can be subject to day-night and seasonal variations, it gives rise to a smooth gamma spectral shape (Baldoncini et al., 2018b) having no peaks interfering with the estimation of ^{214}Pb net photopeak count rates. The attenuation effect on the gamma radiation due to the aluminium box surrounding the NaI(Tl) detector was constant over time and did not affect ^{214}Pb activity measurements. Moreover, potential spectral gain variations due to temperature fluctuations were accounted for energy calibrating each

0.25 h gamma-ray spectrum in order to properly integrate net count rates in the ^{214}Pb photopeak energy window. Measurement conditions were stable and under control during the entire data-taking period as there were no potential anthropic interferences, no surrounding tall trees affecting rainfall estimations and both stations were installed in a homogeneous and morphologically flat terrain. Finally, attention was paid in placing the bucket rain gauge of the agro-meteorological station far enough from the two solar panels to avoid rainfall interception and consequently biased rain amount measurements.

2.3. Experimental data

Among the 42 rains recorded over the 190 days of effective data-taking period (4 April – 2 November, 2017), 12 rain Episodes reported in Table 2 were identified according to the following two criteria: (i)

Table 1

Scheme of the mathematical process used for reconstructing the ^{214}Pb net count rate time series during a rain episode. Every interval of time corresponds to a period P of the episode. The equations in the third column are used sequentially for fitting the count rate $C(t)$ as function of time t (in hours) for obtaining the sudden increase of count rate (ΔC) and the background (C_{Bkg}), knowing λ_{Pb} . The sudden increase of count rate (ΔC_i) depends on the parameters (A , d) as reported in Eq. (7).

Period	Interval of time	Equations
P1	$t < t_1 + \frac{0.25 h}{2}$	$C(t) = C_{\text{Bkg}}^{\text{Before}}$
P2	$t_1 + \frac{0.25 h}{2} \leq t < t_2 + \frac{0.25 h}{2}$	$C(t) = \Delta C_1 e^{-\lambda_{\text{Pb}} \left[t - \left(t_1 + \frac{0.25 h}{2} \right) \right]} + C_{\text{Bkg}}(t)$
	$t_i + \frac{0.25 h}{2} \leq t < t_{i+1} + \frac{0.25 h}{2}$	$C(t) = \Delta C_1 e^{-\lambda_{\text{Pb}} \left[t - \left(t_1 + \frac{0.25 h}{2} \right) \right]} + \dots + \Delta C_i e^{-\lambda_{\text{Pb}} \left[t - \left(t_i + \frac{0.25 h}{2} \right) \right]} + C_{\text{Bkg}}(t)$
	$t_n + \frac{0.25 h}{2} \leq t < t_{n+1} + \frac{0.25 h}{2}$	$C(t) = \Delta C_1 e^{-\lambda_{\text{Pb}} \left[t - \left(t_1 + \frac{0.25 h}{2} \right) \right]} + \dots + \Delta C_n e^{-\lambda_{\text{Pb}} \left[t - \left(t_n + \frac{0.25 h}{2} \right) \right]} + C_{\text{Bkg}}(t)$
P3	$t_{n+1} + \frac{0.25 h}{2} \leq t < t_{n+1} + 4.5 h$	$C(t) = \Delta C_1 e^{-\lambda_{\text{Pb}} \left[t - \left(t_1 + \frac{0.25 h}{2} \right) \right]} + \dots + \Delta C_n e^{-\lambda_{\text{Pb}} \left[t - \left(t_n + \frac{0.25 h}{2} \right) \right]} + C_{\text{Bkg}}^{\text{After}}$
P4	$t \geq t_{n+1} + 4.5 h$	$C(t) = C_{\text{Bkg}}^{\text{After}}$

mean rainfall rate ≥ 3 mm/h and (ii) P2 duration < 4 h (Fig. 6). The first criterion was applied in order to assure the actual observation of a rainfall. Since the rain gauge sensitivity is 0.25 mm and the temporal bin of the model is 0.25 h a threshold rainfall rate of 3 mm/h was conservatively defined. After this selection 14 Episodes were identified. Then we rejected 2 rainfall occurrences which lasted 9.75 and 15.00 h (Fig. 6) since for these long and intermittent rains the assumptions described in Section 2.1 were not valid. The radon-aerosol heterogeneities in the clouds related to the cloud history could have significant impact on estimation of count rate background and model parameters (A and d). Note that it was not necessary to take precautions in case of irrigations concomitant or close in time to rainfalls as irrigation water does not produce any increase in the ^{214}Pb net count rate (see panel 6 of Fig. 8).

The 12 Episodes include globally (P1+P2+P3+P4) 832 temporal bins of 0.25 h each. The minimum and maximum rain duration were respectively 0.75 h and 3.50 h, the minimum and maximum average rainfall rates were respectively 3.0 mm h^{-1} and 13.0 mm h^{-1} , and the minimum and maximum amount of precipitated water in a single episode were respectively 3.8 mm and 23.5 mm (Table 2).

The well-known day-night fluctuation (Greenfield et al., 2002; Sturrock et al., 2018; Wilkening, 1990) is clearly observed in our dataset of ^{214}Pb net count rate: a subset of 15 days is reported in Fig. 7. The average dispersion of the count rate (i.e. maximum-minimum value) is 1.6 cps, corresponding to an average linear variation of 0.13 cps h^{-1} in an interval approximately of 12 h. Considering that the mean standard deviation characterizing a single ^{214}Pb net count rate measurement is 0.22 cps, a background count rate linear variation corresponding to 3 standard deviations (0.66 cps) would be registered in 5 h. This argument justifies the adoption of the 5 h reference time for the estimation of the average ^{214}Pb background net count rates before the beginning and after the end of the rain (see Section 2.1). A further investigation of these fluctuations could shed light on possible sources of periodical signal increase/decrease related for instance to cosmic radiation, radon day/night average concentrations and variations in day/night top-soil moisture levels.

Table 3 reports the ^{214}Pb counting statistics for the 12 rain Episodes. For each 0.25 h temporal bin, individual ^{214}Pb gross count rates were obtained by integrating all events recorded in the (320 – 380) keV

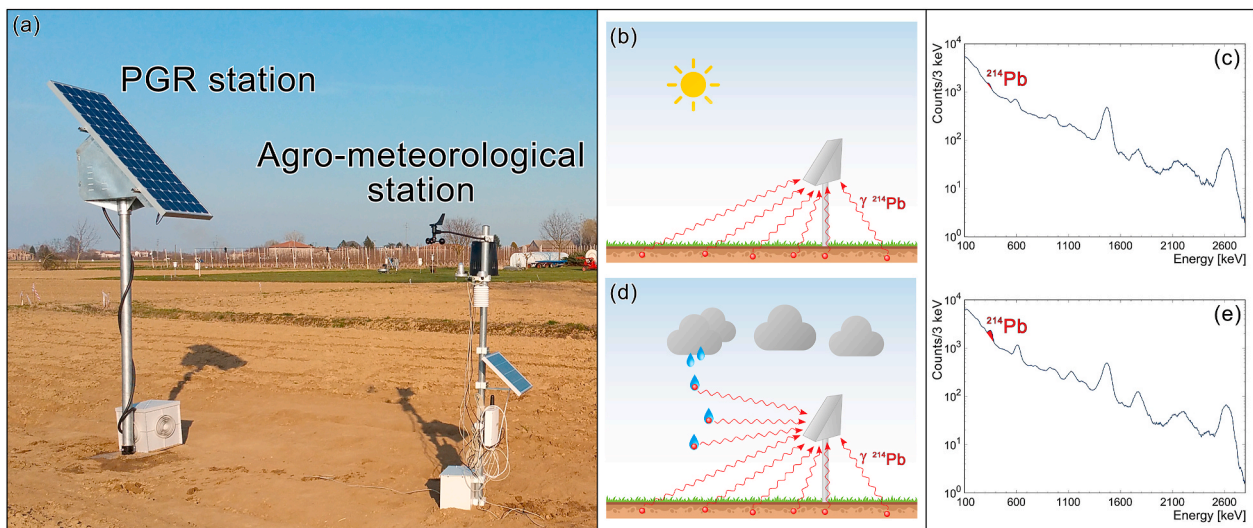


Fig. 5. Panel (a): Proximal Gamma-Ray (PGR) spectroscopy station, equipped with a 1 L NaI(Tl) detector, and agro-meteorological station installed at the test field located in the Emiliano-Romagnolo Canal irrigation district in Emilia Romagna, Italy (44.57° N, 11.53° E, 16 m above sea level). Panels (b) to (e) illustrate the rationale at the basis of rain-induced ^{214}Pb activity measurements through proximal gamma-ray spectroscopy. In absence of rain the detector receives gamma radiation produced in the decay of ^{214}Pb distributed in the soil (panel b) and measures a gamma spectrum (panel c) characterized by a net area in the main ^{214}Pb photopeak (in red) proportional to the ^{214}Pb ground abundance. When it rains, ^{214}Pb atoms in the clouds attach to raindrops (panel d) which, by falling off, generate a rain-induced increase of the ^{214}Pb gamma activity at ground level, experimentally observed as an increase in the ^{214}Pb photopeak net area (panel e). (For interpretation of the references to colour in this figure legend, the reader is referred to the Web version of this article.)

Table 2

Main features of the selected 12 rain Episodes, listed in chronological order. In the columns 3, 4 and 5 are presented the start, end time and duration referred to P2 (see Section 2.1 for the definition). The total precipitation of each episode was estimated by summing individual precipitation amounts recorded over the episode duration. The mean rain rate of each episode was evaluated by dividing the total precipitation amount by the corresponding P2 duration.

Episode	Start Day	P2 Start Time [hh:mm]	P2 End Time [hh:mm]	P2 Duration [h]	Precipitation [mm]	Rate [mm/h]
1	April 16, 2017	23:15	02:00	2.75	8.0	3.0
2	April 27, 2017	21:15	23:30	2.25	7.8	3.4
3	May 04, 2017	23:00	23:45	0.75	6.3	8.3
4	June 25, 2017	13:30	14:15	0.75	3.8	5.1
5	June 28, 2017	18:45	20:15	1.50	15.3	10.2
6	July 11, 2017	15:00	18:15	3.25	23.5	7.2
7	August 06, 2017	18:30	20:15	1.75	18.3	10.4
8	August 10, 2017	13:45	14:45	1.00	13.0	13.0
9	September 02, 2017	22:15	23:00	0.75	3.8	5.1
10	September 07, 2017	23:00	00:45	1.75	5.5	3.1
11	September 24, 2017	12:30	13:45	1.25	9.0	7.2
12	October 06, 2017	16:45	20:30	3.50	19.0	5.1

Table 3

Gross and net counting statistics in the ^{214}Pb photopeak energy window before, during and after Period 2 (P2) for the 12 rain Episodes. The mean ^{214}Pb gross and net background count rates of Period 1 (P1) and Period 4 (P4) are the average and standard deviation of individual count rates measured before and after the rain respectively. The max gross and net ^{214}Pb count rates of P2 + P3 correspond to the maximum gross and net values recorded during the rain periods Period 2 and Period 3. By assuming a Poissonian counting distribution, the uncertainty on the maximum gross count rate in the rain period was estimated as the square root of the gross counts divided by the width of the temporal bin. The uncertainty on the maximum net counts was obtained by combining the Poissonian uncertainty with the uncertainty associated to the background estimation, adapted from Equation 5.42 of (Gilmore, 2008). For the definitions of periods P1, P2, P3 and P4 see Section 2.1 and Fig. 4.

Episode	P1		P2 + P3		P4	
	Mean gross [cps]	Mean net [cps]	Max gross [cps]	Max net [cps]	Mean gross [cps]	Mean net [cps]
1	32.0 ± 0.5	1.3 ± 0.2	46.0 ± 0.2	4.5 ± 0.3	31.1 ± 0.7	1.1 ± 0.2
2	31.0 ± 0.6	1.1 ± 0.2	43.8 ± 0.2	4.9 ± 0.3	30.3 ± 0.5	1.0 ± 0.2
3	31.4 ± 0.7	1.1 ± 0.2	41.2 ± 0.2	4.0 ± 0.2	31.3 ± 0.8	1.1 ± 0.2
4	32.1 ± 0.6	1.2 ± 0.3	49.7 ± 0.2	6.2 ± 0.3	31.3 ± 0.5	1.0 ± 0.2
5	30.7 ± 0.7	1.0 ± 0.3	53.6 ± 0.2	5.6 ± 0.3	29.9 ± 0.5	1.1 ± 0.2
6	29.6 ± 0.6	0.8 ± 0.2	62.0 ± 0.3	7.5 ± 0.3	29.4 ± 0.6	1.0 ± 0.3
7	32.8 ± 1.4	1.4 ± 0.3	73.6 ± 0.3	7.3 ± 0.3	30.2 ± 0.5	1.0 ± 0.2
8	32.0 ± 0.7	1.1 ± 0.2	44.3 ± 0.2	3.9 ± 0.3	28.4 ± 0.6	0.8 ± 0.3
9	32.9 ± 1.6	1.4 ± 0.4	48.7 ± 0.2	4.5 ± 0.3	31.1 ± 0.6	1.0 ± 0.3
10	31.4 ± 0.8	1.0 ± 0.2	50.3 ± 0.2	5.5 ± 0.3	31.1 ± 0.6	0.9 ± 0.2
11	34.4 ± 1.1	1.5 ± 0.3	50.5 ± 0.2	4.3 ± 0.3	31.3 ± 0.5	1.1 ± 0.3
12	34.1 ± 0.8	1.3 ± 0.2	69.2 ± 0.3	6.2 ± 0.3	31.9 ± 0.5	1.1 ± 0.2

photopeak energy window corresponding to the 352 keV gamma emission line. The net ^{214}Pb photopeak area determination was performed according to the trapezoid method described in Section 5.4.1 of (Gilmore, 2008), where a fixed value of 3.5 was adopted for the m parameter, i.e. the mean number of channels on each side of the peak region used to estimate the linear background beneath the peak. Following the approach described in Section 2.1, the ^{214}Pb background count rate before and after the rain time were calculated respectively over P1 and P4 for each rain episode (see also Figs. 5 and 8). They are a baseline

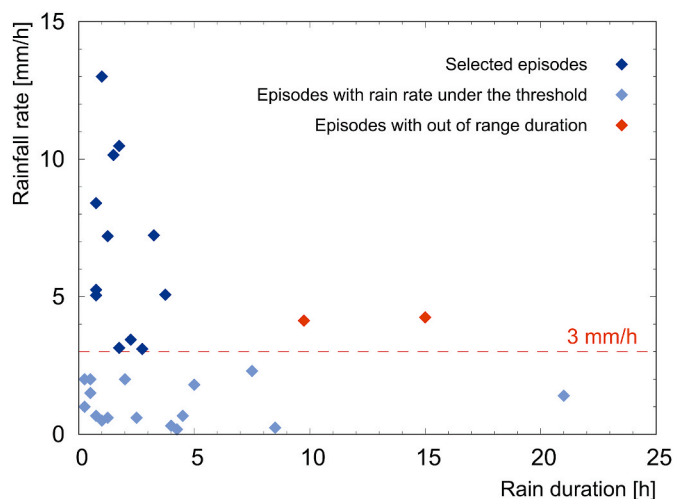


Fig. 6. Scatter plot of the rainfall rate (in mm/h) versus the rain duration (in h) for each of the 42 rains occurred during the data taking period. Note that 13 rains, having the same duration (0.25 h) and rainfall rate (1 mm/h), are indistinguishable in the plot. The first criterion excludes the rains (light blue symbols) with a rainfall rate < 3 mm/h (red dashed line). The second criterion excludes two rains (red symbols) with a duration > 4 h. The dark blue symbols represent the 12 Episode selected for the analysis. (For interpretation of the references to colour in this figure legend, the reader is referred to the Web version of this article.)

representing the ^{214}Pb gamma signal associated with the soil source and a mean atmospheric ^{222}Rn concentration, which is typically affected by a daily modulation (Fig. 7).

The time series of the ^{214}Pb net count rates during each rain episode together with the predictions of the model presented in Section 2.1 are plotted in Fig. 8. As expected, measurements performed with the PGR station are extremely sensitive to rain water but insensitive to irrigation water (Fig. 8, Episode 6). Indeed, contrary to rain droplets, irrigation water does not collect ^{222}Rn daughters and therefore is not responsible for any increase in the ^{214}Pb count rate.

3. Results and discussions

The model was applied against radiometric data measured for each of the 12 rain Episodes (Fig. 8) in order to reconstruct the experimental ^{214}Pb net count rate series and to estimate the best fit values of four free parameters: A , d , C_{Bkg}^{Before} and C_{Bkg}^{After} . For a given rain Episode, the model C given by the equations in Table 1 with parameters $\{A, d, C_{Bkg}^{Before}, C_{Bkg}^{After}\}$ was fitted to M experimental ^{214}Pb net count rates y_m [cps], measured

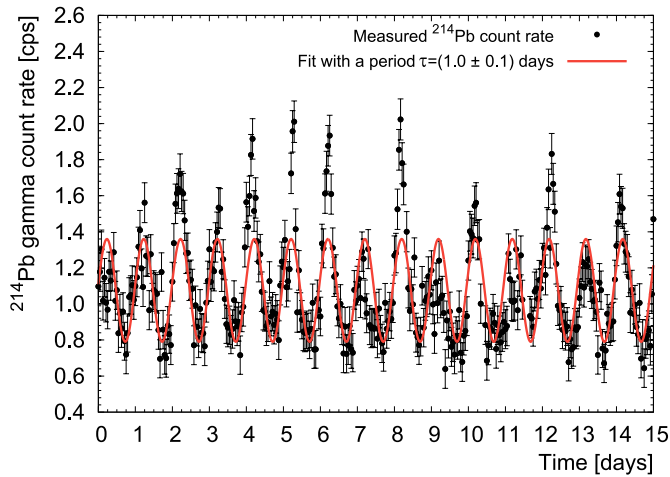


Fig. 7. ^{214}Pb net count rate measured with 1 h temporal resolution over a continuous period of 15 days in absence of irrigation and rainfall fitted with a function (red line) having a period of 1.0 ± 0.1 days. As expected, the maxima and minima signals are recorded, during the selected year period, in the evening ($\sim 17:30$) and in the morning ($\sim 5:30$), respectively. (For interpretation of the references to colour in this figure legend, the reader is referred to the Web version of this article.)

with uncertainty σ_m [cps] at temporal positions t_m [s], by minimizing the following χ^2 function:

$$\chi^2 = \sum_{m=1}^M \frac{\left[y_m - C(t_m; A, d, C_{Bkg}^{Before}, C_{Bkg}^{After}) \right]^2}{\sigma_m^2} \quad (8)$$

where the m index indicates a 0.25 h temporal bin and runs from 1, corresponding to the beginning of P1, up to M , corresponding to the end of P4.

Table 4 summarizes the main results obtained in reconstructing the experimental ^{214}Pb net count rate time series over the 12 rain Episodes according to the model reported in the previous section. The best fit values for the ^{214}Pb background net count rates C_{Bkg}^{Before} and C_{Bkg}^{After} (Table 4), obtained respectively for P1 and P4, are compatible with the corresponding experimental values (Table 2) for each rain episode. As expected, C_{Bkg}^{Before} is generally larger than C_{Bkg}^{After} because of the shielding effect caused by rain water deposited to the ground and penetrated into the soil (Baldoncini et al., 2019). The exception is represented by Episode 6, for which C_{Bkg}^{After} is larger than C_{Bkg}^{Before} , and can be explained considering that irrigation water was distributed to the soil approximately 5 to 3 h prior the beginning of the rain time (panel 6 of Fig. 8).

In order to assess the reliability of the model in predicting the ^{214}Pb gamma activity increase in P2 and the subsequent decrease in P3, the distributions of residuals have been inspected. All the distributions prove centred in 0, allowing to exclude systematic biases in the predictions and confirming a good model accuracy. The corresponding standard deviations are always lower than 0.5 cps, demonstrating the precision of the model estimates.

The linear relation between measured and estimated ^{214}Pb net count rates (Fig. 9a), described by a slope (0.94 ± 0.14) and intercept (0.13 ± 0.21) [cps] with a coefficient of determination $r^2 = 0.93$, proves the good reliability of the model in the reconstructions of the 355 temporal bins of P2 and P3. If we consider only the 139 bins of P2 (Fig. 9b), the fit further improves with resulting value of (0.99 ± 0.19) for the slope and (0.04 ± 0.48) [cps] for the intercept with $r^2 = 0.91$. Slope and intercept values are always respectively compatible with 1 and 0 within 1σ , confirming the exclusion of statistically significant systematics.

As introduced in Section 2.1, the sudden increase of the count rate ΔC

and the gamma activity density G can be analysed as tracers of precipitations. In particular, the model functions built from Eq. (4) and Eq. (5) are adopted to reproduce respectively the ΔC and G dependence on the rain rate R :

$$\Delta C = \Delta T \cdot A \cdot R^d \quad (9)$$

$$G = A \cdot R^{d-1} \quad (10)$$

where for a fixed $\Delta T = 0.25$ h, ΔC and G are obtained with $\{A, d\}_{\Delta C}$ and $\{A, d\}_G$ as free parameters respectively. We analysed 82 temporal bins of P2 characterized by non-zero rainfall amount. The fit of ΔC and G as a function of the rain rate R is shown in Fig. 10 and Fig. 11 and permits us to calculate the best values of $\{A, d\}_{\Delta C}$ and $\{A, d\}_G$.

We note that the best fit parameters $\left\{ A = (2.15 \pm 0.15) \left[\text{cps mm}^{-0.50} \text{h}^{-0.50} \right], d = (0.50 \pm 0.03) \right\}_{\Delta C}$ and $\left\{ A = (1.94 \pm 0.13) \left[\text{cps mm}^{-0.52} \text{h}^{-0.48} \right], d = (0.52 \pm 0.03) \right\}_G$ are completely compatible within 1σ . In the theoretical framework described in Section 2.1, these two independent results prove that rain induced gamma activity and activity density are directly and inversely related to the rain rate respectively. Since the d parameter is detector independent, we emphasize that our result is in excellent agreement with the value $x = (0.5 \pm 0.1)$ published by (Mercier et al., 2009). The variability of A and d values reported in Table 4 can be explained with variations of in-cloud ^{222}Rn concentration and/or of in-cloud scavenging efficiency (Mercier et al., 2009).

Results shown in Fig. 10 confirm that the sudden increase of ΔC is positively correlated with the rain rate R ($\Delta C \propto R^{1/2}$), which implies that the more intense is the precipitation, the higher is the count rate increase recorded by the PGR station. Similarly, results presented in Fig. 11 show that the ^{214}Pb gamma activity density G is inversely correlated with the rain rate R ($G \propto R^{-1/2}$), which means that, being equal the total precipitation amount, the lower is the rainfall intensity (i.e. the longer is the rain duration), the higher is the radioactive content of rain water. For instance, although Episode 12 and 7 were characterized by approximately the same amount of precipitated water (Table 2), Episode 12 had about half the mean rain rate of Episode 7 but a larger overall ^{214}Pb gamma activity increase, as can be inferred from the ^{214}Pb net count rate time series over the rain time (Fig. 8).

These evidences appear even clearer by studying the activity density G as a function of the droplet diameter. Following (Villermaux and Bossa, 2009), the rain rate R can be linked to the average droplet diameter $\langle \lambda \rangle$ [cm] by the relation:

$$\langle \lambda \rangle = k \cdot R^{\frac{2}{9}} \quad (11)$$

where $k = \frac{1}{48.5} \left[\text{cm} \cdot \left(\frac{\text{mm}}{\text{h}} \right)^{-2/9} \right]$. By substituting Eq. (11) in Eq. (10), it is possible to infer the correlation between the activity density G as a function of the average droplet diameter $\langle \lambda \rangle$:

$$G = A \cdot R^{d-1} = A \cdot \left[\left(\frac{\langle \lambda \rangle}{k} \right)^{\frac{9}{2}} \right]^{d-1} = A \cdot \left(\frac{\langle \lambda \rangle}{k} \right)^{\frac{9}{2}(d-1)} \quad (12)$$

By substituting the best fit parameters $\{A = (1.94 \pm 0.13) [\text{cps mm}^{-0.52} \text{h}^{-0.48}], d = (0.52 \pm 0.03)\}_G$ (Fig. 11) in Eq. (12), it is possible to obtain the following relation:

$$G = 1.94 \cdot \left(\frac{\langle \lambda \rangle}{k} \right)^{\frac{9}{2}(0.52-1)} = 4.43 \cdot 10^{-4} \cdot \langle \lambda \rangle^{-2.16} \quad (13)$$

where G is expressed in $\left[\frac{\text{cps}}{\text{mm}} \right]$ and $\langle \lambda \rangle$ in [cm]. However, frequency in raindrop size distributions is usually based upon volume rather than number: it is useful to define a median volume diameter λ_m , which divides the larger and smaller drops of the distribution into two groups of equal volume (Laws and Parsons, 1943). By assuming an exponential

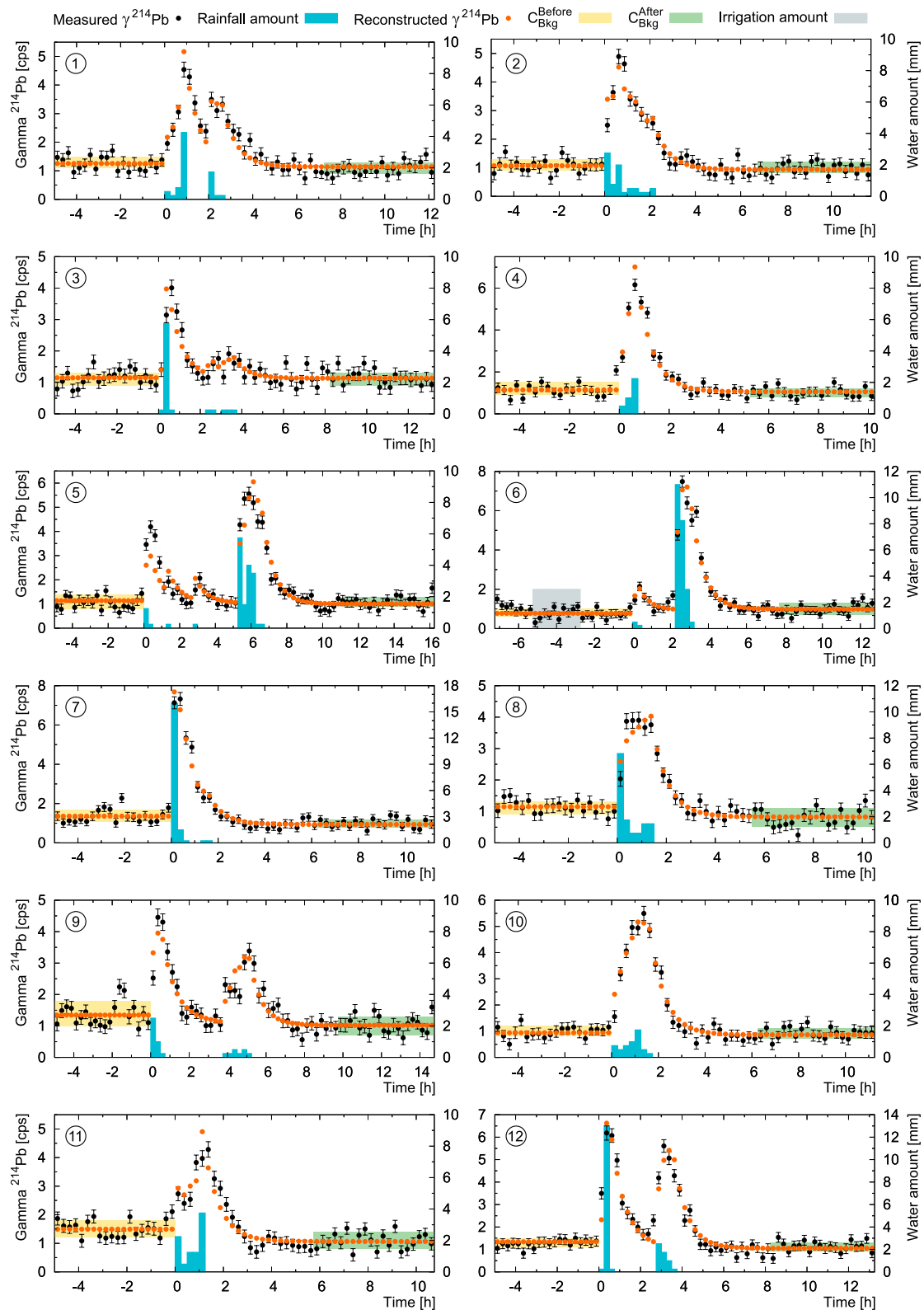


Fig. 8. Time series of the ^{214}Pb net count rates for the 12 rain Episodes. For each episode, the black dots represent the net count rates measured in the ^{214}Pb photopeak energy window, together with their uncertainties, while the orange dots correspond to the net count rates predicted by the model. The yellow (green) bands are the 1σ -interval of the average net count rates estimated in P1 (P4) (see also Table 3 and Fig. 3). Blue and grey bars report the amount of rainfall and irrigation water, respectively. Episode 6 shows an irrigation which, as expected, does not produce any increase in the ^{214}Pb net count rate. The drizzles (rain rate < 3 mm/h) which occurred before (Episode 5) or after (Episodes 3 and 9) the main rain episode were not defined as rain Episodes but were considered for the ^{214}Pb net count rate time series reconstruction. (For interpretation of the references to colour in this figure legend, the reader is referred to the Web version of this article.)

Table 4

Best fit parameters obtained by applying the model reported in Section 2.1 to fit the experimental ^{214}Pb net count rate time series measured during the 12 rain Episodes, listed in chronological order (see also Fig. 8). The first and second columns identify respectively the rain Episode number and date. In the third column are reported the mean and the standard deviation associated to the distribution of residuals ($y_m - C(t_m)$) see Eq. (8) obtained from the fit function in P2 and P3. The last four columns report respectively the best fit values of the A , d , $C_{\text{Bkg}}^{\text{Before}}$ and $C_{\text{Bkg}}^{\text{After}}$ free parameters, together with their estimation uncertainty, obtained after the χ^2 minimization procedure.

Episode	Date	Residuals [cps]	$A \pm \delta A$ [cps mm ^d h ^{d-1}]	$d \pm \delta d$	$C_{\text{Bkg}}^{\text{Before}} \pm \delta C_{\text{Bkg}}^{\text{Before}}$	$C_{\text{Bkg}}^{\text{After}} \pm \delta C_{\text{Bkg}}^{\text{After}}$
1	April 16, 2017	0.05 ± 0.28	2.6 ± 1.0	0.48 ± 0.06	1.25 ± 0.05	1.14 ± 0.04
2	April 27, 2017	-0.03 ± 0.32	1.5 ± 0.6	0.77 ± 0.06	1.07 ± 0.05	0.94 ± 0.04
3	May 04, 2017	0.01 ± 0.32	1.0 ± 0.4	0.75 ± 0.07	1.15 ± 0.05	1.13 ± 0.04
4	June 25, 2017	0.02 ± 0.37	5.4 ± 3.2	0.42 ± 0.09	1.14 ± 0.05	1.05 ± 0.04
5	June 28, 2017	-0.03 ± 0.37	3.4 ± 0.7	0.34 ± 0.03	1.14 ± 0.04	1.00 ± 0.03
6	July 11, 2017	-0.02 ± 0.34	2.5 ± 0.5	0.48 ± 0.04	0.77 ± 0.05	0.99 ± 0.04
7	August 06, 2017	-0.04 ± 0.31	1.4 ± 0.3	0.71 ± 0.05	1.36 ± 0.05	0.94 ± 0.05
8	August 10, 2017	0.04 ± 0.26	3.4 ± 0.2	0.16 ± 0.09	1.15 ± 0.05	0.83 ± 0.04
9	September 02, 2017	0.00 ± 0.32	2.6 ± 1.0	0.48 ± 0.05	1.35 ± 0.05	1.02 ± 0.04
10	September 07, 2017	-0.07 ± 0.30	4.6 ± 3.7	0.23 ± 0.11	0.94 ± 0.05	0.86 ± 0.04
11	September 24, 2017	-0.02 ± 0.41	0.7 ± 0.6	0.99 ± 0.15	1.50 ± 0.05	1.06 ± 0.04
12	October 06, 2017	0.03 ± 0.37	4.0 ± 0.8	0.39 ± 0.03	1.34 ± 0.05	1.05 ± 0.04

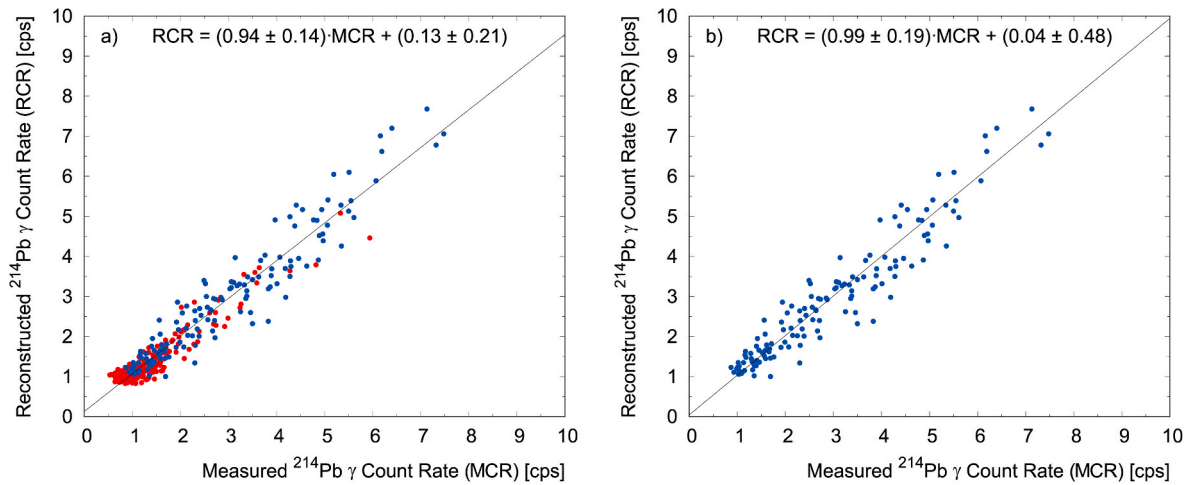


Fig. 9. The ^{214}Pb net Reconstructed Count Rate (RCR) versus the ^{214}Pb net Measured Count Rate (MCR) are reported together with the linear regression (black lines) considering only statistical uncertainties. The coefficient of determination obtained fitting the 355 temporal bins of P2 (blue dots) and of P3 (red dots) is $r^2 = 0.93$ (panel a). Analysing the 139 temporal bins of P3, the coefficient of determination is $r^2 = 0.91$. (For interpretation of the references to colour in this figure legend, the reader is referred to the Web version of this article.)

drop size distribution (Villiermaux and Bossa, 2009), the median volume diameter λ_m can be linked to the average droplet diameter $\langle \lambda \rangle$ as (Eq. (5) of (Ulbrich and meteorology, 1983) with $\mu = 0$):

$$\lambda_m = 3.67 \cdot \langle \lambda \rangle \quad (14)$$

As depicted in Fig. 12, it is hence possible to express the relation between the activity density $G \left[\frac{\text{cps}}{\text{mm}} \right]$ and the median volume diameter $\lambda_m [\text{cm}]$:

$$G = 7.35 \cdot 10^{-3} \cdot \lambda_m^{-2.16} \quad (15)$$

4. Conclusions

In this work we present an exhaustive study of the radon daughters' gamma activity measured at the ground in relation to rain rate. The results shown in this paper have been achieved by analysing data acquired for 7 months with a proximal gamma-ray spectroscopy detector and an agro-meteorological station installed in a test field. We summarize here the main conclusions of this paper.

- i) A reproducible mathematical model was developed for reconstructing the temporal evolution of the ^{214}Pb net count rate

during rain episodes as function of the rain rate R . The reliability of the method was confirmed by two relevant results. The predicted ^{214}Pb net count rates, 5 h before the rainfall and 5 h after the ^{214}Pb exponential decrease post-rainfall, are in agreement at 1σ level with the measured values (Tables 3 and 4). The ^{214}Pb signals reconstructed by the model are linearly correlated with the values measured during the rain time with a coefficient of determination $r^2 = 0.91$. Moreover, the slope and the intercept coefficients are compatible within 1σ with 1 and 0 respectively (Fig. 9).

- ii) The sudden increase of ^{214}Pb count rates (ΔC) observed during every rainfall is clearly related to the rain rate (R) by the power law $\Delta C = A \cdot R^d$, where $A = (2.15 \pm 0.15) [\text{cps mm}^{-0.50} \text{h}^{-0.50}]$ is an equipment dependent parameter. The calculated universal parameter $d = (0.50 \pm 0.03)$ proves that the expected increase of radon daughters' activity at the ground due to rainfalls depends on the square root of the rain rate (Fig. 10).
- iii) For a fixed rainfall amount, the lower is the rainfall intensity (i.e. the longer is the rain duration), the higher is the radon daughters' content in the rain water (i.e. the ^{214}Pb activity density G). We observed a power law dependence $G = A \cdot R^{d-1}$ between the ^{214}Pb gamma activity density $G \left[\frac{\text{cps}}{\text{mm}} \right]$ and the rain rate R (Fig. 11). The

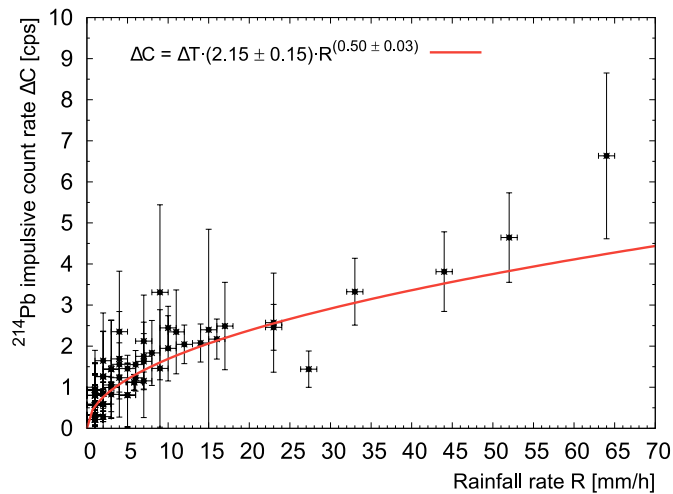


Fig. 10. Plot of the sudden increase of ^{214}Pb count rate ΔC as function of the rainfall rate R . The ΔC values were calculated over all the 82 temporal bins ($\Delta T = 0.25$ h) of P2 characterized by non-zero rainfall amounts. The best fit curve in red was obtained using Eq. (9) as model function. (For interpretation of the references to colour in this figure legend, the reader is referred to the Web version of this article.)

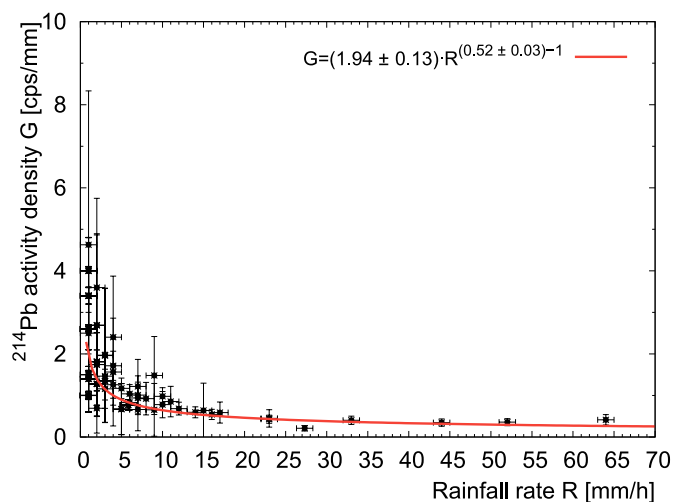


Fig. 11. Plot of the ^{214}Pb activity density G as function of the rainfall rate R . The G values were calculated over all the 82 temporal bins ($\Delta T = 0.25$ h) of P2 characterized by non-zero rainfall amounts. The best fit curve in red was obtained using Eq. (10) as model function. (For interpretation of the references to colour in this figure legend, the reader is referred to the Web version of this article.)

best fit parameters $A = (1.94 \pm 0.13) [\text{cps mm}^{-0.52} \text{ h}^{-0.48}]$ and $d = (0.52 \pm 0.03)$ agree with those obtained by an independent analysis in ii).

- iv) Studying the ^{214}Pb activity density G as a function of droplet size, we can conclude that radon daughters' abundance in a rain droplet is inversely proportional to the rain median volume diameter λ_m , according to the following function: $G = 7.35 \cdot 10^{-3} \cdot \lambda_m^{-2.16}$. This experimental evidence shows that the smaller droplets have on average higher radon daughters' abundances.

We shall learn more about the rain formation and scavenging mechanisms from future refined gamma measurements at the ground, including ^{214}Bi data. Using the data from the network of thousands of gamma sensors distributed on the ground (typically utilised for

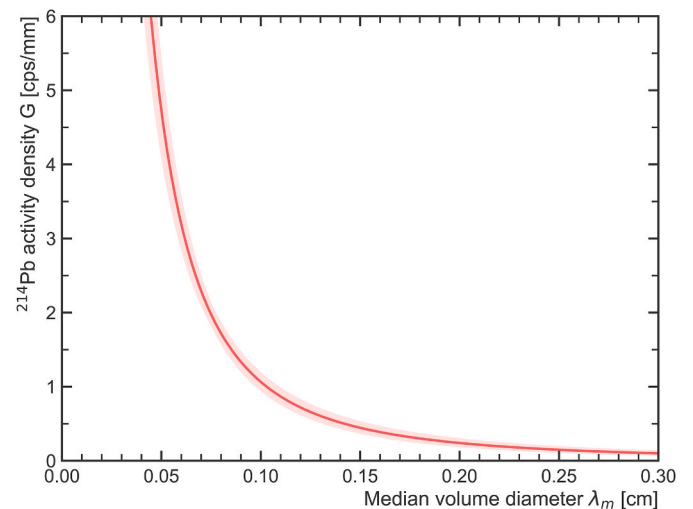


Fig. 12. The activity density G [cps/mm] of ^{214}Pb nuclei in raindrops as a function of the median volume diameter λ_m [cm] follows a curve (red line) described by Eq. (15). The shaded pink line shows the uncertainty due to the standard deviations of the best fit parameters of Fig. 11. (For interpretation of the references to colour in this figure legend, the reader is referred to the Web version of this article.)

monitoring the air radioactivity in case of nuclear fallout) or radiation portal monitors, the activity density of the rain could provide valuable information to cloud science. Finally, further studies could exploit the presented model to assess the impact of the rain induced radiation on absorbed outdoor dose rates.

Declaration of competing interest

The authors declare that they have no known competing financial interests or personal relationships that could have appeared to influence the work reported in this paper.

CRediT authorship contribution statement

Carlo Bottardi: Conceptualization, Methodology, Software, Validation, Formal analysis, Writing - original draft, Writing - review & editing, Visualization. **Matteo Albéri:** Investigation, Writing - review & editing, Conceptualization. **Marica Baldoncini:** Writing - original draft, Writing - review & editing. **Enrico Chiarelli:** Software, Data curation, Formal analysis, Writing - review & editing. **Michele Montuschi:** Writing - review & editing, Resources, Methodology, Conceptualization. **Kassandra Giulia Cristina Raptis:** Investigation, Writing - review & editing, Visualization. **Andrea Serafini:** Writing - review & editing, Visualization, Data curation, Software. **Virginia Strati:** Conceptualization, Writing - review & editing, Visualization, Project administration, Funding acquisition. **Fabio Mantovani:** Writing - review & editing, Conceptualization, Visualization, Supervision, Project administration, Funding acquisition.

Acknowledgments

This work was partially funded by the National Institute of Nuclear Physics (INFN) through the ITALian RADioactivity project (ITALRAD) and by the Theoretical Astroparticle Physics (TAsP) research network. The authors would like to acknowledge the support of the Project "Protocolli Operativi Scalabili per l'agricoltura di precisione - POSITIVE"- CUP: D41F1800080009 and of the University of Ferrara (FAR 2019–2020). The authors thank the staff of GeoExplorer Impresa Sociale s.r.l. for its support and Stefano Anconelli, Gabriele Baroni, Giovanni Fiorentini, Claudio Pagotto, Domenico Solimando, Laura Tositti for their

collaboration which made possible the realization of this study.

Appendix A. Supplementary data

Supplementary data to this article can be found online at <https://doi.org/10.1016/j.atmosenv.2020.117728>.

References

- Baldoncini, M., Albéri, M., Bottardi, C., Chiarelli, E., Raptis, K.G.C., Strati, V., Mantovani, F., 2018a. Investigating the potentialities of Monte Carlo simulation for assessing soil water content via proximal gamma-ray spectroscopy. *J. Environ. Radioact.* 192, 105–116.
- Baldoncini, M., Albéri, M., Bottardi, C., Chiarelli, E., Raptis, K.G.C., Strati, V., Mantovani, F.J.G., 2019. Biomass Water Content Effect on Soil Moisture Assessment via Proximal Gamma-Ray Spectroscopy, vol. 335, pp. 69–77.
- Baldoncini, M., Albéri, M., Bottardi, C., Minty, B., Raptis, K.G.C., Strati, V., Mantovani, F., 2017. Exploring atmospheric radon with airborne gamma-ray spectroscopy. *Atmos. Environ.* 170, 259–268.
- Baldoncini, M., Albéri, M., Bottardi, C., Minty, B., Raptis, K.G.C., Strati, V., Mantovani, F., 2018b. Airborne gamma-ray spectroscopy for modeling cosmic radiation and effective dose in the lower atmosphere. *IEEE Trans. Geosci. Rem. Sens.* 56, 823–834.
- Barbosa, S.M., Miranda, P., Azevedo, E.B., 2017. Short-term variability of gamma radiation at the ARM eastern north atlantic facility (azores). *J. Environ. Radioact.* 172, 218–231.
- Baskaran, M., 2016. *Radon: A Tracer for Geological, Geophysical and Geochemical Studies*. Springer International Publishing.
- Bossev, P., Cinelli, G., Hernández-Ceballos, M., Cernohlavek, N., Gruber, V., Dehandschutter, B., Menneson, F., Bleher, M., Stöhlker, U., Hellmann, I., Weiler, F., Tollefsen, T., Tognoli, P.V., de Cort, M., 2017. Estimating the terrestrial gamma dose rate by decomposition of the ambient dose equivalent rate. *Journal of environmental radioactivity* 166, 296–308.
- Castleman, A.W., 1991. Consideration of the chemistry of radon progeny. *Environ. Sci. Technol.* 25, 730–735.
- Chambers, S.D., Galeriu, D., Williams, A.G., Melintescu, A., Griffiths, A.D., Crawford, J., Dyer, L., Duma, M., Zorila, B., 2016. Atmospheric stability effects on potential radiological releases at a nuclear research facility in Romania: characterising the atmospheric mixing state. *J. Environ. Radioact.* 154, 68–82.
- Chambers, S.D., Wang, F., Williams, A.G., Xiaodong, D., Zhang, H., Lonati, G., Crawford, J., Griffiths, A.D., Ianniello, A., Allegrini, I., 2015. Quantifying the influences of atmospheric stability on air pollution in Lanzhou, China, using a radon-based stability monitor. *Atmos. Environ.* 107, 233–243.
- Eatough, J.P., Henshaw, D.L., 1995. The theoretical risk of non-melanoma skin cancer from environmental radon exposure. *J. Radiol. Prot.* 15, 45–51.
- Friedmann, H., 2012. Radon in earthquake prediction research. *Radiat. Protect. Dosim.* 149, 177–184.
- Froehlich, K., 2009. *Environmental Radionuclides: Tracers and Timers of Terrestrial Processes*. Elsevier.
- Gilmere, G.R., 2008. *Practical Gamma-Ray Spectrometry*. John Wiley & Sons, Ltd, Chichester, UK.
- Greenfield, M., Domondon, A., Okamoto, N., Watanabe, I., 2002. Variation in γ -ray count rates as a monitor of precipitation rates, radon concentrations, and tectonic activity. *Journal of applied physics* 91, 1628–1633.
- Greenfield, M.B., Ito, N., Iwata, A., Kubo, K., Ishigaki, M., Komura, K., 2008. Determination of rain age via γ rays from accreted radon progeny. *J. Appl. Phys.* 104, 074912.
- Harrison, R.G., Aplin, K.L., Rycroft, M.J., 2014. Brief Communication: earthquake–cloud coupling through the global atmospheric electric circuit. *Nat. Hazards Earth Syst. Sci.* 14, 773–777.
- Hopke, P.K., 1989. Use of electrostatic collection of ^{218}Po for measuring Rn. *Health Phys.* 57, 39–42.
- Inomata, Y., Chiba, M., Igarashi, Y., Aoyama, M., Hirose, K., 2007. Seasonal and spatial variations of enhanced gamma ray dose rates derived from ^{222}Rn progeny during precipitation in Japan. *Atmos. Environ.* 41, 8043–8057.
- Jacob, D.J., Prather, M.J., 1990. Radon-222 as a test of convective transport in a general circulation model. *Tellus B* 42, 118–134.
- Jacob, D.J., Prather, M.J., Rasch, P.J., Shia, R.-L., Balkanski, Y.J., Beagley, S.R., Bergmann, D.J., Blackshear, W.T., Brown, M., Chiba, M., Chipperfield, M.P., de Grandpré, J., Dignon, J.E., Feichter, J., Genthon, C., Grose, W.L., Kasibhatla, P.S., Köhler, I., Kritz, M.A., Law, K., Penner, J.E., Ramonet, M., Reeves, C.E., Rotman, D.A., Stockwell, D.Z., Van Velthoven, P.F.J., Verver, G., Wild, O., Yang, H., Zimmermann, P., 1997. Evaluation and intercomparison of global atmospheric transport models using ^{222}Rn and other short-lived tracers. *J. Geophys. Res.* 102, 5953–5970.
- Karangelos, D.J., Petropoulos, N.P., Anagnostakis, M.J., Hinis, E.P., Simopoulos, S.E., 2005. Data Leading to the Investigation of a Relation between Seismic Activity and Airborne Radon Decay Product Concentrations Outdoors, Radioactivity in the Environment. Elsevier, pp. 187–197.
- Kendall, G.M., Smith, T.J., 2002. Doses to organs and tissues from radon and its decay products. *J. Radiol. Prot.* 22, 389–406.
- Laws, J.O., Parsons, D.A.J.E., Transactions American Geophysical Union, 1943. The Relation of Raindrop-size to Intensity, vol. 24, pp. 452–460.
- Livesay, R.J., Blessinger, C.S., Guzzardo, T.F., Hausladen, P.A., 2014. Rain-induced increase in background radiation detected by Radiation Portal Monitors. *J. Environ. Radioact.* 137, 137–141.
- Melintescu, A., Chambers, S., Crawford, J., Williams, A., Zorila, B., Galeriu, D., 2018. Radon-222 related influence on ambient gamma dose. *Journal of environmental radioactivity* 189, 67–78.
- Mercier, J.F., Tracy, B.L., d'Amours, R., Chagnon, F., Hoffman, I., Korpach, E.P., Johnson, S., Ungar, R.K., 2009. Increased environmental gamma-ray dose rate during precipitation: a strong correlation with contributing air mass. *J. Environ. Radioact.* 100, 527–533.
- Minato, S., 1980. Analysis of time variations in natural background gamma radiation flux density. *J. Nucl. Sci. Technol.* 17, 461–469.
- Mostafa, M., Khalaf, H., Zhukovsky, M., 2020. Radon decay products equilibrium at different aerosol concentrations. *Appl. Radiat. Isot.* 156.
- Muraki, Y., Axford, W.I., Matsubara, Y., Masuda, K., Miyamoto, Y., Menjou, H., Sakakibara, S., Sako, T., Takami, T., Yamada, T., 2004. Effects of atmospheric radiation on cosmic rays. *Phys. Rev. D* 69, 123010.
- Paatero, J., 2000. Wet deposition of radon-222 progeny in northern Finland measured with an automatic precipitation gamma analyser. *Radiat. Protect. Dosim.* 87, 273–280.
- Porstendörfer, J., 1994. Properties and behaviour of radon and thoron and their decay products in the air. *J. Aerosol Sci.* 25, 219–263.
- Riggio, A., Santulin, M., 2015. *Earthquake Forecasting: a Review of Radon as Seismic Precursor*. BGTA.
- Shapiro, M.H., Forbes-Resha, J.L., 1975. $^{214}\text{Bi}/^{214}\text{Pb}$ ratios in air at a height of 20 m. *J. Geophys. Res.* 80, 1605–1613.
- Stevanović, N., Nikežić, D., Djordjević, A., 2004. The recoil factor of. *J. Aerosol Sci.* 35, 1041–1050.
- Strati, V., Albéri, M., Anconelli, S., Baldoncini, M., Bittelli, M., Bottardi, C., Chiarelli, E., Fabbri, B., Guidi, V., Raptis, K., Solimando, D., Tomei, F., Villani, G., Mantovani, F., 2018. Modelling soil water content in a tomato field: proximal gamma ray spectroscopy and soil–crop system models. *Agriculture* 8, 60.
- Sturrock, P., Steinitz, G., Fischbach, E.J.A.P., 2018. Analysis of Gamma Radiation from a Radon Source. II: Indications of Influences of Both Solar and Cosmic Neutrinos on Beta Decays, vol. 100, pp. 1–12.
- Takeyasu, M., Iida, T., Tsujimoto, T., Yamasaki, K., Ogawa, Y., 2006. Concentrations and their ratio of ^{222}Rn decay products in rainwater measured by gamma-ray spectrometry using a low-background Ge detector. *J. Environ. Radioact.* 88, 74–89.
- Turekian, K.K., Graustein, W.C., 2003. *Natural Radionuclides in the Atmosphere, Treatise on Geochemistry*. Elsevier, pp. 261–279.
- Ulbrich, C.W., 1983. Natural variations in the analytical form of the raindrop size distribution. *Journal of climate and applied meteorology* 22, 1764–1775.
- Villiermaux, E., Bossa, B., 2009. Single-drop fragmentation determines size distribution of raindrops. *Nat. Phys.* 5, 697–702.
- Wilkening, M., 1981. *Radon in Atmospheric Studies: a Review*. New Mexico Inst. of Mining and Technology.
- Wilkening, M., 1990. *Radon in the Environment*, vol. 40. Elsevier. Studies in Environmental Science.
- Woith, H., 2015. Radon earthquake precursor: a short review. *Eur. Phys. J. Spec. Top.* 224, 611–627.
- Yakovleva, V.S., Nagorsky, P.M., Cherepnev, M.S., Kondratyeva, A.G., Ryabkina, K.S., 2016. Effect of precipitation on the background levels of the atmospheric β - and γ -radiation. *Appl. Radiat. Isot.* 118, 190–195.
- Yoshioka, K., 1992. The seasonal variation of rainout activity of short-lived radon daughters. *Radiat. Protect. Dosim.* 45, 395–398.